Article

Polymer-Embedded Silver Microgrids by Particle-Free Reactive Inks for Flexible High-Performance Transparent Conducting Electrodes

Ziyu Zhou, S. Brett Walker, Melbs LeMieux, and Paul W. Leu*

Cite This: *ACS Appl. Electron. Mater.* 2021, 3, 2079−2086

Read Online

ACCESS | 📊 Metrics & More | 📰 Article Recommendations | 🆘 Supporting Information

ABSTRACT: We report on the fabrication and characterization of polymer-embedded silver (Ag) microgrid structures using a particle-free reactive Ag ink for flexible high-performance transparent conductive electrodes. The Ag microgrids are cured at low temperatures and embedded directly into flexible polyethylene terephthalate (PET) films to create structures needed for high transparency and low sheet resistance. The conductive grids demonstrate 91.8% transmission and a sheet resistance of 0.88 Ω/sq corresponding to an optical conductivity ratio σ_{dc}/σ_{op} of nearly 4500 with gridlines of 10 μm width. The microgrids may be fabricated with gridlines down to 3.5 μm width. The fabrication of microgrids from a particle-free reactive ink results in several enhancements compared to microgrids fabricated from particle-based conductive Ag inks. The use of particle-free ink offers about 2.5 times higher conductivity, over 3 times lower surface roughness, and better stability under mechanical adhesion, bending, and folding tests. Our results demonstrate the following: (1) a scalable approach to microgrid manufacturing, (2) microgrids with nearly the best transparent electrode performance properties, and (3) the clear benefit of the paradigm of particle-free conductive inks compared to conventional nanoparticle inks.

KEYWORDS: *reactive silver ink, nanoparticle ink, transparent conducting electrode, photolithography, reactive-ion etching*
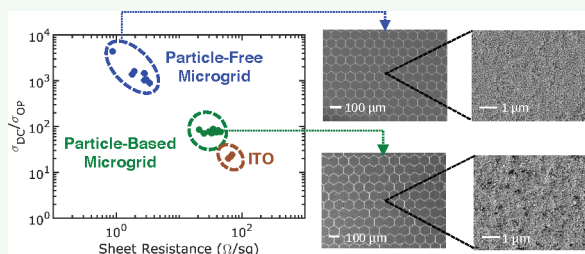
INTRODUCTION

Indium tin oxide (ITO) is utilized in most transparent conductor applications because of its high optical transparency and low electrical resistivity.[1] However, for emerging flexible optoelectronics, its performance on flexible polymers such as polyethylene terephthalate (PET) is inadequate, as ITO cannot be annealed under high temperature, and thus, achieving sheet resistances (R_s) under 10 Ω/sq is difficult. Commercialized ITO on PET substrates has demonstrated R_s ranging from 10 to 300 Ω/sq for a transparency T of 85 to 90% in the ultraviolet to visible region[2] and R_s = 50 Ω/sq with T = 84% at 550 nm wavelength.[3] Furthermore, ITO is a brittle material not suitable for flexible optoelectronic applications. As ITO films are bent, microscopic cracks begin to form, and their sheet conductance decreases.[4] ITO also suffers from the limited availability of indium and costly, time-consuming deposition methods.[5,6] ITO is commercially deposited by DC-magnetron sputtering, which requires high energy consumption, a vacuum environment, and expensive equipment.[7] ITO-replacement materials have been extensively investigated to address these shortcomings and have included metal nanowires,[8−11] metal nanomeshes,[12−14] graphene,[15,16] and conductive polymers.[17,18]

Among these alternatives, there is great interest in metal microgrids. Metal microgrids exhibit a uniformly low sheet resistance, and their transmission and sheet resistance can be controlled by varying the microgrid width, pitch, and thickness.

Moreover, metal microgrids can be fabricated with a variety of metals with different work functions for integration with disparate semiconductors across many applications.[19] Metal microgrids can also be integrated with ITO alternatives such as metal nanomeshes, graphene, or conductive polymers.[7,20,21] The fabrication techniques of metal microgrids on both rigid and flexible substrates have been extensively studied, including lithography patterning with metal evaporation[7] or sputtering,[22] laser direct writing,[23] and ink-based methods such as inkjet printing,[24] gravure printing,[25] and electrohydrodynamic jet printing.[26]

However, these fabrication methods face several challenges. In order to achieve low sheet resistance without compromising transparency, microgrids with high aspect ratios of large thickness and small width are needed. However, achieving high aspect ratios is difficult with microgrid fabrication methods such as evaporation, sputtering, or laser direct writing. Ink-based methods have trouble achieving high aspect ratios, as the ink tends to spontaneously spread across the substrate. Furthermore, a large thickness or large roughness of the

2079
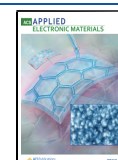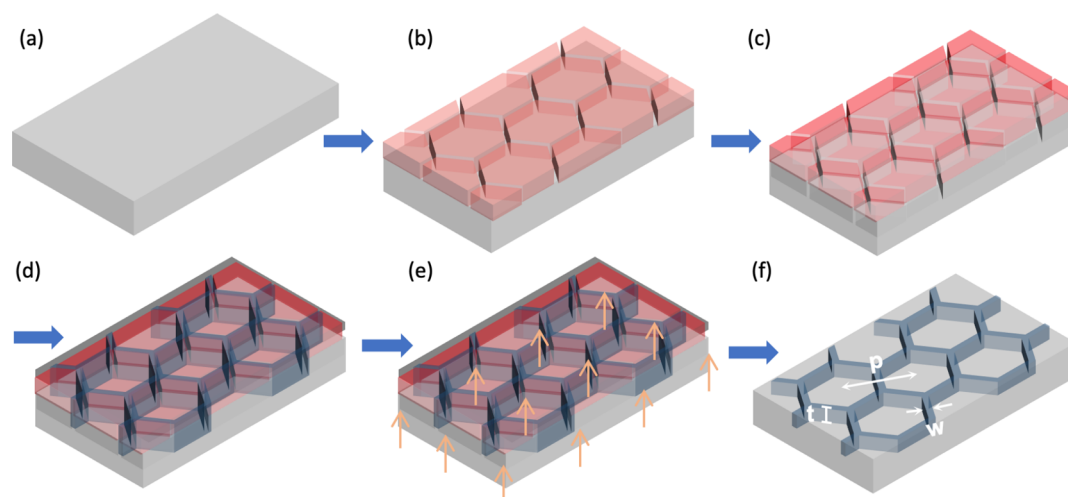
Figure 1. Process flow schematic for creating flexible PET-embedded Ag microgrids: (a) flexible transparent PET substrate, (b) photolithography, (c) reactive-ion etching, (d) metal ink spin-coating, (e) Ag ink curing, and finally (f) lift-off. The Ag microgrids are hexagonal arrays embedded into a flexible PET substrate defined by pitch p, thickness t, and width w.

metal microgrids may result in short-circuiting in optoelectronic devices where the active layer is thin.[24] The thickness of the active layer in some organic devices is less than 100 nm.

Recent studies have demonstrated the creation of substrate-embedded metal microgrids for transparent electrodes using particle-based metal inks.[27,28] However, high-temperature sintering is not possible on polymeric substrates, and this leads to issues with voids between metal nanoparticles and high-resistance interfaces that result in low electrical conductivity.[29] Substrate-embedded metal microgrids fabricated with a hexagonal period of 150 μm, groove depth of about 2 μm, and groove width of about 3 μm demonstrated T = 89% in the visible light range and R_s = 4.7 Ω/sq.[27] Another metal microgrid with a hexagonal period of 140 μm, residual depth of 1.8 μm, and groove width of 2.4 μm exhibited a T = 88.6% and R_s = 2.1 Ω/sq.[28] Additionally, nanoparticle-based inks have unsuitable roughness for some optoelectronic devices such that an additional polishing step may be needed to create a smooth surface.[30] Finally, the use of nanoparticle-based inks results in poor adhesion, downstream reliability issues, and poor mechanical stability for the cured metal and the substrate.[31]

Walker et al. has demonstrated a particle-free Ag ink with higher conductivity compared to nanoparticle Ag[29] and a low curing temperature that may be integrated with plastics such as PET.[32] In this paper, we demonstrate the fabrication of Ag microgrids using a similar metal-complex-based particle-free Ag ink and demonstrate its performance advantages compared to microgrids fabricated from particle-based inks. Microgrids embedded in flexible PET substrates were fabricated from a particle-free ink and exhibited high optical transparency T = 91.8% at 550 nm and R_s = 0.88 Ω/sq. The microgrids have a pitch of 300 μm, width of 10 μm, and thickness of 2 μm. The cured particle-free ink metal microgrids have a conductivity as high as 1.7×10^7 S/m, which is 27% of bulk Ag conductivity compared to a conductivity as high as 5.5×10^6 S/m or 8.7% of bulk Ag conductivity for cured Ag nanoparticle ink microgrids. The Ag microgrid exhibits a smaller root-mean-square roughness R_q of 10 nm compared to nanoparticle-based samples with an R_q of 35 nm. We employed a simple spin-coating method to deposit the Ag inks into patterned trenches

and cured the particle-free ink under low temperature (120 °C). The fabrication process was developed with scale-up manufacturing in mind: the Ag ink deposition can be deposited on the film in a roll-to-roll coating method. Furthermore, we found that the embedded Ag microgrids have improved mechanical stability compared to ITO thin films deposited on the PET under adhesion/peeling, bending, and folding.

Metal microgrids fabricated from the particle-free ink demonstrate an improved reliability under 10 tape adhesion and peeling cycles, 200 bending cycles, and 12 folding cycles compared to metal microgrids fabricated from a particle-based ink. For tape adhesion tests, after 10 tape adhesion/peel-off cycles, R_s changes 1.5% for particle-free fabricated microgrids compared to 3.4% for microgrids fabricated from particle-based metal inks after 10 tape adhesion/peel-off cycles. For microgrids fabricated from particle-free inks, the R_s increase after 200 cycles of tension and compression bending is 12.5 and 5.5%, while for the particle-based fabricated samples, the R_s increase is 23.6 and 24.9%, respectively. For folding tests, after 12 folding cycles, the R_s increase for particle-free fabricated microgrids is 126 as compared to 158% for microgrids fabricated from particle-based metal inks. Our results demonstrate (1) a scalable approach to microgrid manufacturing, (2) microgrids with nearly the best transparent electrode performance properties, and (3) the clear benefit of particle-free conductive inks compared to conventional nanoparticle inks in terms of optoelectronic performance, lower roughness, and better stability under mechanical deformation.

■ EXPERIMENTAL SECTION

Microscale Ag Grid Fabrication. Polymer-embedded Ag microgrids were fabricated using photolithography and lift-off by both particle-free reactive ink and particle-based conductive ink. Polyethylene terephthalate (PET) substrates were cleaned and prebaked on a hot plate at 120 °C for 2 min. A 2 μm thick photoresist AZ4210 from MicroChemicals was then spin-coated onto the substrate followed by a soft-bake at 120 °C for 3 min. The photoresist was exposed (Quintel Q4000 MA Mask Aligner) and developed in diluted AZ400 K (1:4) from MicroChemicals for 60 s. Reactive-ion etching (RIE; Trion Phantom III) with 45 sccm CF$_4$ and 5 sccm O$_2$ was used to dry-etch the pattern into the PET to create trenches. Particle-free Ag ink (EI710 from Electroninks) was first
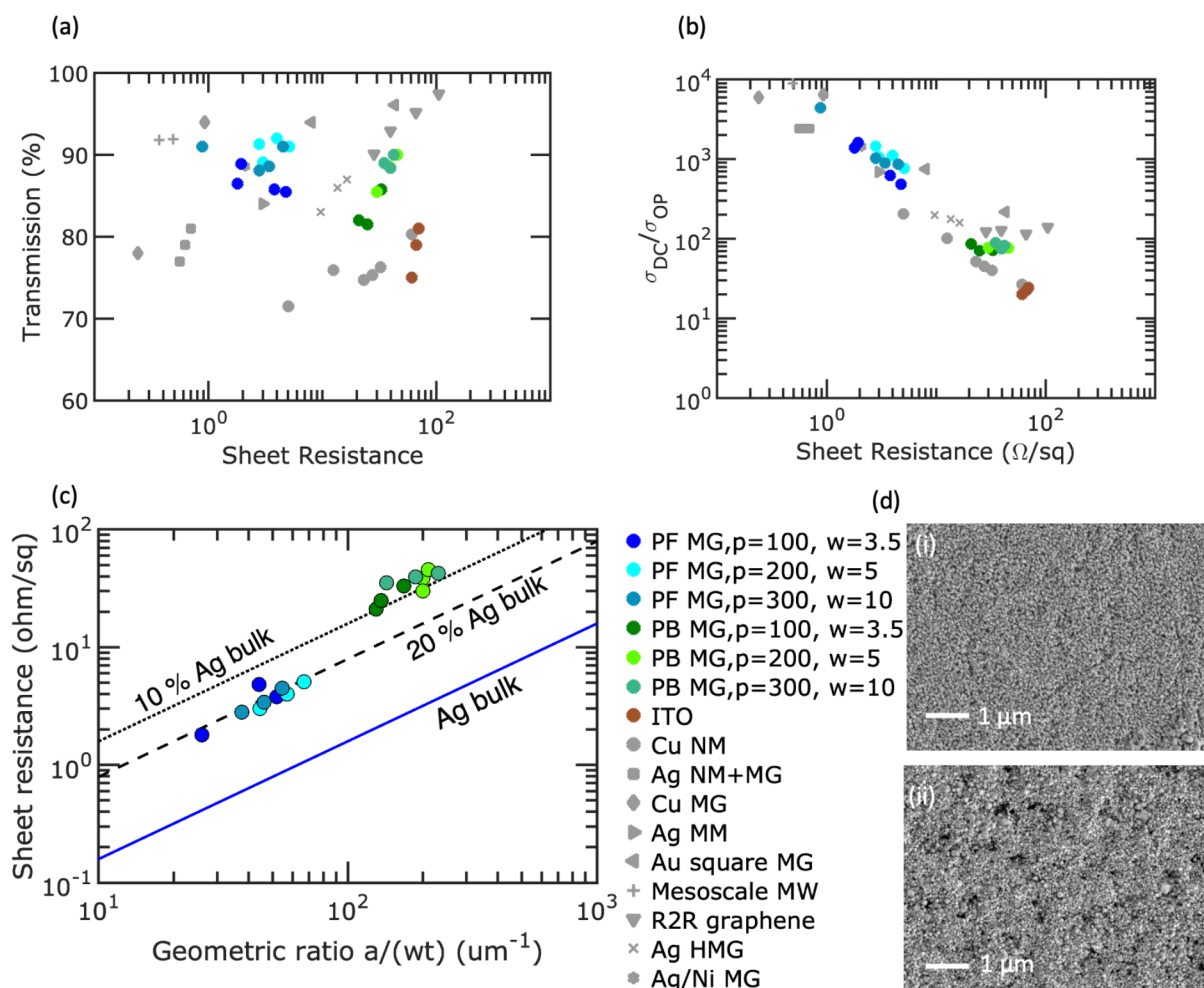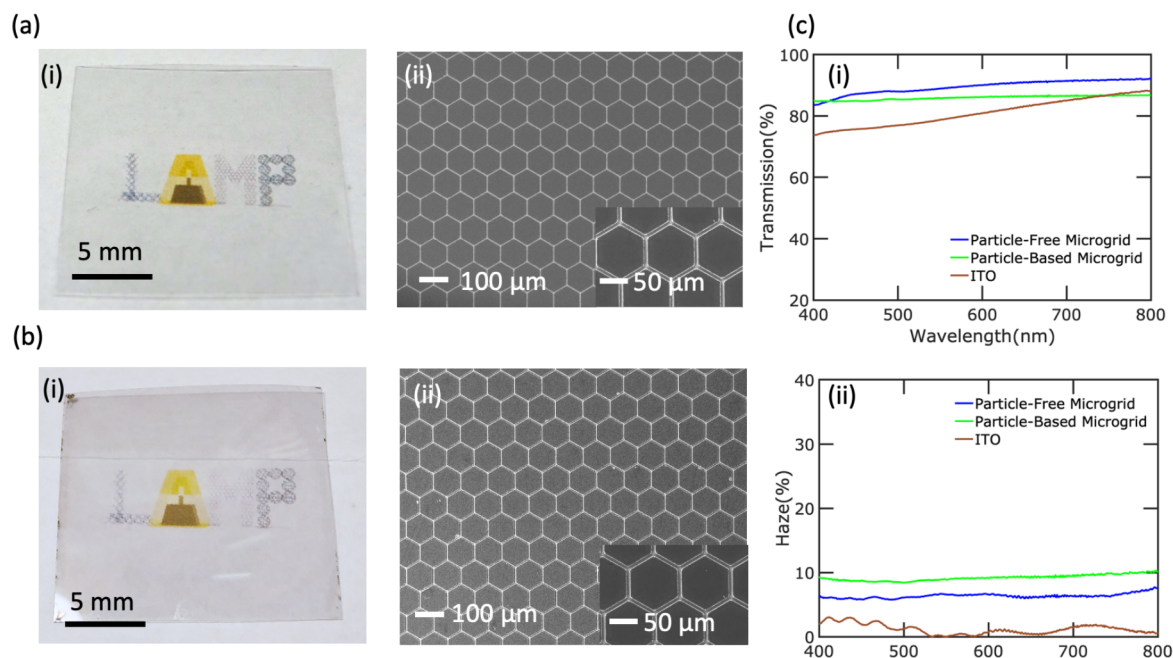
Figure 2. Performance for PET-embedded Ag microgrids compared to ITO and other transparent conductors on PET in the literature. (a) Transmission versus sheet resistance for various transparent conductors. Particle-free metal microgrids (PF MGs) and particle-based metal microgrids (PB MGs) of various pitch and width are shown. (b) Figure of merit σ_{DC}/σ_{OP} of PET-embedded Ag microgrids compared with other transparent conductors. (c) Relative conductivity (compared to bulk Ag) for various transparent conductors as a function of geometric ratio. (d) Top view of (i) particle-free ink microgrid and (ii) particle-based ink Ag microgrid.

deposited onto the patterned photoresist by spin-coating at 2000 rpm followed by a cure process at 120 °C for 5 min. And then, a second spin-coating at 2000 rpm was applied to improve the trench filling. The final cure was at 120 °C for 20 min. For comparison, a particle-based Ag ink (Smart Ink S-CS01130 with a <50 nm Ag nanoparticle size[33]) was deposited onto the patterned photoresist by spin-coating at 2000 rpm followed by curing at 120 °C for 5 min. A second spin-coating at 2000 rpm was applied afterward followed by a final cure at 120 °C for 30 min. Then, the photoresist was removed using 1165 remover at room temperature with gentle ultrasonication, cleaning, and drying for both samples.

Materials Characterization. Sheet resistance measurements were carried out by a probe station with a semiconductor device analyzer (B1500A Semiconductor Device Analyzer from Keysight Technologies). The van der Pauw method was used for sheet resistance characterization. The morphology characteristics of the fabricated polymer-embedded Ag microgrid were investigated using scanning electron microscopy (Zeiss SIGMA VP). The surface roughness of the samples was characterized by atomic force microscopy (Veeco Multimode V and Dimension V SPM). The total transmittance and haze spectrum of fabricated microgrids were measured at wavelengths from 250 to 1200 nm using a UV−vis−NIR spectrometer with a 60 mm diameter integrating sphere (PerkinElmer Lambda 750).

■ RESULTS AND DISCUSSION

Figure 1 shows the process flow schematic for creating flexible PET-embedded Ag microgrids. The processing begins with a flexible PET substrate (Figure 1(a)) that is spin-coated with a layer of photoresist and patterned by photolithography (Figure 1(b)). The pattern is then transferred to the substrate by reactive-ion etching (RIE) (Figure 1(c)). Then, Ag ink is applied to the PET by spin-coating. Both reactive particle-free Ag inks and particle-based Ag inks were evaluated for comparison purposes. Scanning electron microscopy (SEM) images showing the surface topography of thin films formed from particle-free ink and particle-based ink on PET are included in Supplemental Figure S1. By spin-coating, the Ag ink was easily deposited onto the substrate (Figure 1(d)). The particle-free microgrid was cured at a temperature of 120 °C for 5 min for partial curing and following another spin-coating step, cured at 120 °C for 20 min. The particle-based microgrid was cured in an oven at a temperature of 120 °C for 5 min for partial curing and then at 120 °C for 30 min for final curing after a second coating of ink (Figure 1(e)). Finally, the photoresist was lifted off (Figure 1(f)). Figure 1(f) shows the schematic of the substrate-embedded microgrids, which are hexagonal arrays defined by pitch *p*, width *w*, and thickness *t*.

Figure 3. Particle-free microgrid and particle-based microgrid comparison. (a) Appearance of particle-free microgrid from (i) optical image and (ii) overhead SEM. (b) Appearance of particle-based microgrid from (i) optical image and (ii) overhead SEM. (c)(i) Transmittance and (ii) haze spectra of Ag microgrids embedded directly on flexible PET and ITO on PET.

PET-embedded Ag microgrids of various pitch (p) and width (w) were fabricated. Figure 2 demonstrates the performance of fabricated Ag microgrid samples compared to other transparent conductors on PET in the literatures. Figure 2(a) presents the transmission versus sheet resistance. The data for microgrids formulated by particle-free reactive ink of different pitches and widths (p = 100 μm, w = 3.5 μm; p = 200 μm, w = 5 μm; and p = 300 μm, w = 10 μm) are colored with different shades of blue. The data for microgrids formulated by particle-based conductive ink of different pitches and widths (p = 100 μm, w = 3.5 μm; p = 200 μm, w = 5 μm; and p = 300 μm, w = 10 μm) are plotted with different shades of green. The data of ITO on PET is shown with brown data points. In addition to our data, we plot the performance of other transparent conductors on flexible PET in the literature, including copper nanomeshes (Cu NMs),[12] Ag nanomeshes and microgrids (Ag NMs + MGs),[7] copper microgrids (Cu MGs),[34] Ag micromeshes (Ag MMs),[35] Au square microgrids (MGs),[26] mesoscale metal wires (MWs),[36] roll-to-roll graphene (R2R graphene),[37] Ag hierarchical microgrids (Ag HMGs),[38] and Ag/Ni microgrids (MGs).[30] The transmission is shown at wavelength λ = 550 nm, and the effect of the substrate is excluded. Our particle-free Ag microgrid samples exhibit an R_s between 1 to 5 Ω/sq with a T of 85% to 91%. In contrast, the particle-based Ag grid samples show worse R_s and transparency, with an R_s of 21 to 45 Ω/sq and T of 81 to 90% (at 550 nm). Furthermore, the PET-embedded Ag microgrids exhibit superior transmittance and sheet resistance compared to other transparent conductors in the literature, except for mesoscale metal wires. Mesoscale metal wires demonstrated by the Cui group have a large cross section area, which enables low sheet resistance without sacrificing transparency.[36] However, these metal wires may suffer from large surface roughness that is unsuitable for some optoelectronic applications. Our best sample demonstrates R_s = 0.88 Ω per sq with T = 91.8%. Figure 2(b) plots the figure of merit σ_{dc}/σ_{op}

versus R_s for the same transparent conductors where σ_{dc} is the dc conductivity, and σ_{op} is the optical conductivity. The figure of merit is related to T and R_s by

$$T = \left(1 + \frac{Z_0}{2R_s}\frac{\sigma_{op}}{\sigma_{dc}}\right)^{-2}$$

where Z_0 = 377 Ω is the free space impedance.[39] Most of our microgrids achieve figures of merit over 500 including some demonstrations over 2000 for a microgrid pitch size of 300 μm and width of 10 μm. These figure of merit values are much higher than those demonstrated by particle-based ink formulated microgrids with a pitch size of 100 μm and grid width of 3.5 μm, which only achieve a figure of merit of 100. In contrast, ITO has a σ_{dc}/σ_{op} under 100. In Figure 2(c), the relative conductivities of microgrid samples are plotted compared to bulk Ag, with three lines plotted as benchmarks. The geometric ratio is defined as p/wt with units of μm^{-1}. For each sample, a conductivity was estimated based on the pitch, diameter, and thickness of the microgrid. The particle-free microgrid has a relative conductivity of 20.7 $\pm$ 3.0% bulk Ag, while the particle-based microgrid has a relative conductivity of 8.4 $\pm$ 1.3% bulk Ag. The highest conductivity for cured particle-free ink metal microgrids is 1.7×10^7 S/m or 27% that of bulk Ag compared to the highest conductivity for particle-based metal microgrids of 5.5×10^6 S/m or 8.7% that of bulk Ag. The particle-free ink is a solution of metal complex in solvent[32] as opposed to a dispersion of inorganic nanoparticles in a polymer/binder/surfactant matrix. Because there are no polymers or surfactants in the particle-free inks, Ag microgrids cured from particle-free ink (Figure 2(d)(i)) have less voids and defects compared to microgrids fabricated from particle-based inks (Figure 2(d)(ii)) and thus are able to achieve higher conductivities.

Figure 3 shows the results from a representative Ag microgrid structure with p = 100 μm, w = 3.5 μm, and a
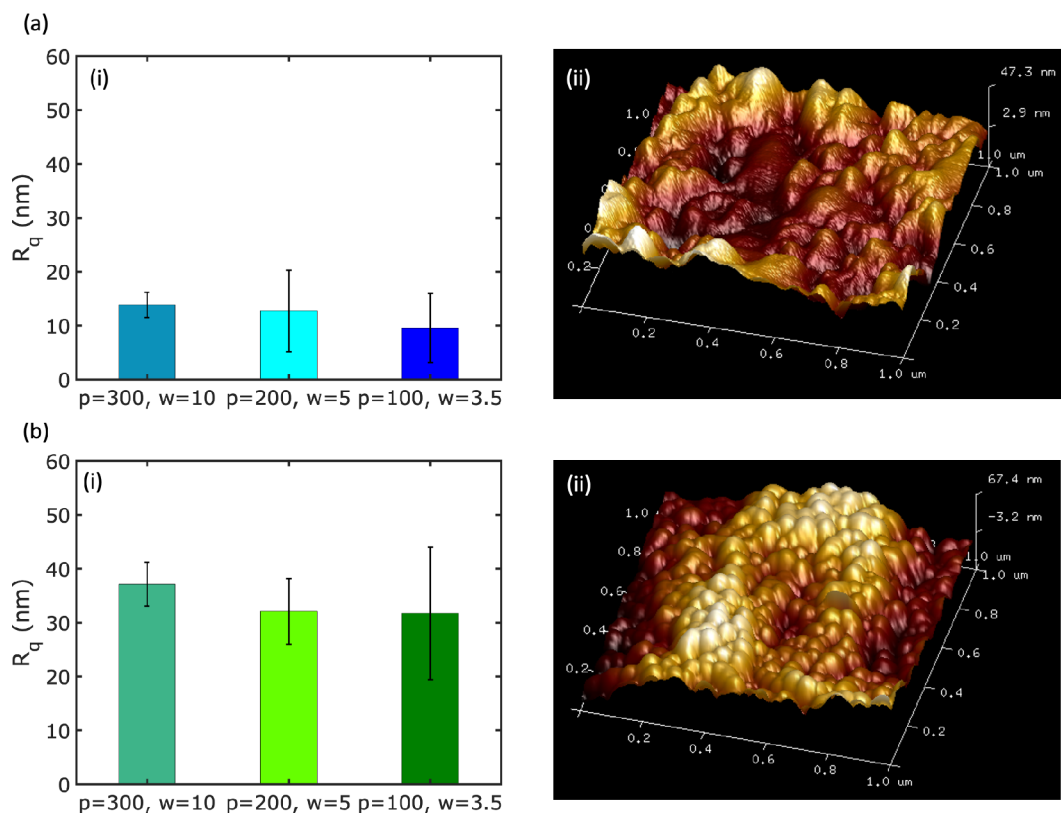
Figure 4. Roughness R_q of particle-free microgrid and particle-based microgrid samples. (a,b)(i) Root-mean-square roughness R_q of particle-free ink and particle-based ink formulated Ag microgrid. The pitch p and width w of the microgrids are listed in microns. (ii) 3D atomic force microscope results of particle-free ink and particle-based ink formulated Ag microgrid ($p = 300$ μm, $w = 10$ μm) surface roughness.

thickness of 1.2 μm. Figure 3(a) shows (i) optical and (ii) SEM overview images of the particle-free microgrid. The sample looks uniform and clear, without the appearance of moiré fringes over an area of about 2 × 2 cm. SEM images of the high uniformity and long-range order of the structure are apparent in Figure 3(a)(ii). For comparison, (b)(i) optical and (ii) SEM overview images of the particle-based microgrid are also shown. The transparency of the metal microgrids strongly depends on their open space, and thus, microgrids fabricated with the particle-free and particle-based inks have comparable transparency. However, the main difference in performance is in the cured Ag conductivity as discussed above. In order to improve the conductivity, the particle-based microgrid may be cured at a higher temperature of 150 °C in order to sinter the particles together. However, the use of a higher temperature leads to lift-off issues, resulting in a large amount of residual metal around the edges of the microgrid and worse transparency. Photoresists are generally soft-baked at 90 to 120 °C after spin-coating to drive off solvents and solidify the photoresist film. The use of a higher curing temperature of 150 °C increases the conductivity from 8.4 ± 1.3% at 120 °C to 8.9 ± 2.2%. However, the transparency decreases from a range of 81 to 90% when cured at 120 °C to a range of 58 to 87% when cured at 150 °C due to the presence of Ag residual (Supplemental Figure S2(d)). Figure 3(c) also compares the (i) transmission spectrum and (ii) haze spectrum of the particle-free microgrid, particle-based microgrid, and experimentally deposited ITO (on PET). The particle-free microgrid exhibits an $R_s = 2.1$ Ω/sq with $T = 89\%$ at 550 nm, while the particle-based microgrid has an $R_s = 24.9$ Ω/sq with $T = 86\%$ at 550 nm. ITO has an R_s of 70 Ω/sq at $T = 80\%$ at a 550

nm wavelength. In Figure 3(c), the haze of the Ag microgrid structure is compared to ITO. The haze is defined as the fraction of total transmission that deviates from the incident beam direction greater than 2.5° as defined by the American Society for Testing and Materials (ASTM) standard D1003.[40] The microgrid embedded in PET has a slight increase in haze compared to the ITO due to light scattering off its nonplanar features. Low haze is desirable for displays, but high haze is desirable for solar cells and light emitting diodes. The metal microgrids may be integrated with various ultrahigh transparency, low haze or ultrahigh transparency, ultrahigh haze glass or plastic substrates depending on the optoelectronic application.[46]

For some optoelectronic devices such as OLEDs, device layers less than 100 nm are deposited onto transparent conductors. The larger roughness may cause current leakage or even result in device failure.[41] Microgrids fabricated from particle-free inks and particle-based inks were compared for their surface roughness R_q, which is the root-mean-square roughness determined from deviations from a baseline. In Figure 4(a,b)(i), the R_q of the particle-free microgrid and particle-based microgrid is plotted. For all the sizes of grids, the R_q of the particle-free ink formulated microgrid is around 10 nm, which is much lower than that of the particle-based ink microgrid sample where the R_q is about 35 nm. In the atomic force microscopy plot of the particle-free microgrid (Figure 4(a)(ii), the surface can be seen to feature larger Ag grains that are responsible for its larger roughness as opposed to the particle-based microgrid (Figure 4(b)(ii). The average roughness R_a shows the same trend as R_q, which is presented in Supplementary Figure S3.
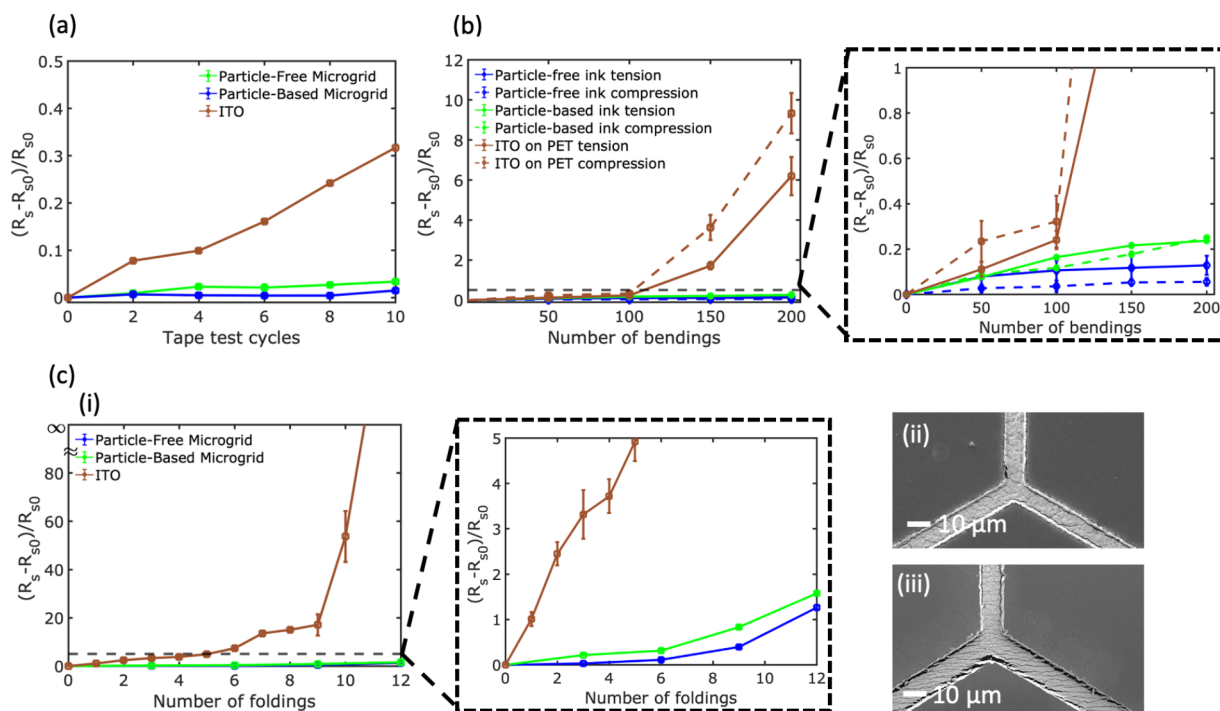
Figure 5. Durability tests for flexible transparent conductors. Relative sheet resistance change of particle-free ink formulated microgrid and particle-based ink formulated microgrid as well as ITO for (a) adhesion/peel-off cycles, (b) bending cycles, and (c)(i) folding cycles. (c) SEM images of (ii) particle-free ink formulated microgrid and (iii) particle-based ink formulated microgrid after 12 folding cycles.

To evaluate the mechanical durability of the embedded microgrid structures for flexible optoelectronics, the performance of the metal microgrids fabricated from particle-free and particle-based inks was monitored under tape adhesion, bending, and folding tests and compared with ITO (Figure 5). These tests were performed on microgrids and ITO fabricated on an ultrathin 1 × 1 cm PET of 25 μm thickness. Figure 5(a) shows the change in sheet resistance under tape adhesion and peel-off tests. The Ag microgrids have a pitch of $p = 300$ μm and width of $w = 10$ μm. The tape tests were applied by adhering Scotch tape to the Ag microgrid or ITO and then peeling off. The transmittance does not change after the peel-off. Figure 5(a) shows the results of the tape tests. Compared to ITO, which has its sheet resistance increase by 31.7%, the sheet resistance change is 1.5% for particle-free fabricated microgrids and 3.4% for microgrids fabricated from particle-based metal ink formulated microgrids.

Bending tests were additionally performed on Ag microgrids and PET. Figure 5(b) shows the results of these bending tests. The Ag microgrid has a pitch of $p = 300$ μm and width of $w = 10$ μm. The sheet resistance was monitored in bending tests where the samples were bent around a rod with 6 mm in diameter, and the sheet resistance was measured every 50 cycles. The compression/tension tests were applied by bending the Ag grid side toward/away from the steel rod. The relative sheet resistance change ($\Delta R_s/R_{s0}$) of ITO increases significantly after 200 cycles in contrast to the Ag microgrids in both tension and compression cases. The relative sheet resistance of the ITO increases by 6.2 and 9.3 times the original sheet resistance of 70 Ω/sq in tension and compression, respectively. The initial cracking in ITO is formed at defect sites such as pin-holes.[42] With repeated bending, these cracks grow, and the resistance increases. In contrast, the Ag microgrid can endure repeated bending without the resistance changing as much as

sputtered ITO on PET, as Ag has a higher yield strength compared to ITO. The critical stress for cracking ITO is $\sigma_c = 0.58$ MPa,[43] much smaller than the tensile stress of Ag, which is 140 MPa.[44] For the particle-free microgrid, the original resistance of the prepared samples for tension and compression tests is 8.8 and 8.4 Ω/sq, respectively. After 200 cycles of bending, the resistance of the samples increases to 9.9 (12.5%) and 8.9 Ω/sq (5.5%) in tension and compression, respectively. For particle-based microgrids, the original resistance of the prepared samples for tension and compression tests is 42.5 and 35.3 Ω/sq, respectively. After 200 cycles of bending, the resistance of the samples increases to 52.5 (23.6%) and 44.1 Ω/sq (24.9%) in tension and compression, respectively.

Figure 5(c)(i) shows the results of folding tests performed on the particle-free microgrid, particle-based microgrid, and ITO. The folds are performed where the transparent conductors are on the inside of the fold. The embedded microgrid has a pitch size of 300 μm and width size of 10 μm. The original sheet resistances are 7.3 and 39.6 Ω/sq for the particle-free microgrid and particle-based microgrid, respectively. After 12 folds, the ITO sample is no longer conductive, where the sheet resistance increases to infinity. This is due to the deep and large cracks that appeared during the folding process. In contrast, the Ag microgrids still maintain their conductivity after 12 folds. For the particle-free microgrid, the resistance increased by 3 and 126% after 3 times and 12 times of folding, respectively, while for the particle-based microgrid, the resistance increased by 31 and 158% after 3 times and 12 times of folding, respectively. Figure 5(c)(ii,iii) shows the cracks within particle-free and particle-based ink formulated microgrid samples after 12 folding cycles. As discussed earlier with regard to higher conductivities, the particle-free microgrids have less voids and defects compared to microgrids fabricated from particle-based inks. These structures thus have

better fracture strength, as fracture tends to happen at interfaces between the grains or nanoparticles.[45] More cracking is observable within the particle-based microgrid as well as delamination between the edge of the microgrid and the polymer.

CONCLUSION

We report on a Ag microgrid embedded in flexible PET film fabricated utilizing particle-free conductive ink to demonstrate a high-performance transparent conductor. The embedded Ag microgrid has good uniformity and ordering and exhibits up to 91.8% transmission at 550 nm and a low sheet resistance of 0.88 Ω/sq. The Ag microgrids fabricated from particle-free Ag inks exhibited enhanced mechanical stability of performance compared to both ITO and Ag microgrids fabricated from particle-based inks in adhesion, bending, and folding tests. Compared to the particle-based Ag ink, the particle-free ink formed microgrids exhibit better transparent electrode performance, lower roughness, and better mechanical durability for flexible optoelectronic applications.

ASSOCIATED CONTENT

Ⓢ Supporting Information

The Supporting Information is available free of charge at https://pubs.acs.org/doi/10.1021/acsaelm.1c00107.

> Figure S1, showing the SEM images for Ag thin film formulated via particle-free and particle-based ink. Figure S2, the demonstration of the performance for PET-embedded Ag microgrids compared to ITO and other transparent conductors on PET in the literature. Figure S3, presenting the average roughness R_a for different microgrid samples (PDF)

AUTHOR INFORMATION

Corresponding Author

Paul W. Leu − *Department of Industrial Engineering, University of Pittsburgh, Pittsburgh, Pennsylvania 15213, United States*; Email: pleu@pitt.edu

Authors

Ziyu Zhou − *Department of Mechanical Engineering and Materials Science, University of Pittsburgh, Pittsburgh, Pennsylvania 15213, United States*; ⓞ orcid.org/0000-0002-1009-9433

S. Brett Walker − *Electroninks Incorporated, Austin, Texas 78744, United States*

Melbs LeMieux − *Electroninks Incorporated, Austin, Texas 78744, United States*

Complete contact information is available at:
https://pubs.acs.org/10.1021/acsaelm.1c00107

Notes

The authors declare no competing financial interest.

ACKNOWLEDGMENTS

REFERENCES

(1) Granqvist, C. G.; Hultåker, A. Transparent and Conducting Ito Films: New Developments and Applications. *Thin Solid Films* **2002**, *411*, 1−5.

(2) Lee, H. B.; Jin, W.-Y.; Ovhal, M. M.; Kumar, N.; Kang, J.-W. Flexible Transparent Conducting Electrodes Based on Metal Meshes for Organic Optoelectronic Device Applications: a Review. *J. Mater. Chem. C* **2019**, *7*, 1087−1110.

(3) Xia, Y.; Sun, K.; Ouyang, J. Highly Conductive Poly (3, 4-Ethylenedioxythiophene): Poly (styrene Sulfonate) Films Treated with an Amphiphilic Fluoro Compound as the Transparent Electrode of Polymer Solar Cells. *Energy Environ. Sci.* **2012**, *5*, 5325−5332.

(4) Chen, Z.; Cotterell, B.; Wang, W.; Guenther, E.; Chua, S. A Mechanical Assessment of Flexible Optoelectronic Devices. *Thin Solid Films* **2001**, *394*, 201−205.

(5) Angmo, D.; Krebs, F. C. Flexible ITO-free polymer solar cells. *J. Appl. Polym. Sci.* **2013**, *129*, 1−14.

(6) Coutal, C.; Azema, A.; Roustan, J.-C. Fabrication and characterization of ITO thin films deposited by excimer laser evaporation. *Thin Solid Films* **1996**, *288*, 248−253.

(7) Gao, T.; Li, Z.; Huang, P.-s.; Shenoy, G. J.; Parobek, D.; Tan, S.; Lee, J.-k.; Liu, H.; Leu, P. W. Hierarchical Graphene/metal Grid Structures for Stable, Flexible Transparent Conductors. *ACS Nano* **2015**, *9*, 5440−5446.

(8) Tokuno, T.; Nogi, M.; Karakawa, M.; Jiu, J.; Nge, T. T.; Aso, Y.; Suganuma, K. Fabrication of Silver Nanowire Transparent Electrodes at Room Temperature. *Nano Res.* **2011**, *4*, 1215−1222.

(9) Rathmell, A. R.; Wiley, B. J. The Synthesis and Coating of Long, Thin Copper Nanowires to Make Flexible, Transparent Conducting Films on Plastic Substrates. *Adv. Mater.* **2011**, *23*, 4798−4803.

(10) Gao, T.; Leu, P. W. Copper nanowire arrays for transparent electrodes. *J. Appl. Phys.* **2013**, *114*, 063107.

(11) Gao, T.; Leu, P. W. The Role of Propagating Modes in Silver Nanowire Arrays for Transparent Electrodes. *Opt. Express* **2013**, *21*, A419.

(12) Gao, T.; Wang, B.; Ding, B.; Lee, J.-k.; Leu, P. W. Uniform and Ordered Copper Nanomeshes by Microsphere Lithography for Transparent Electrodes. *Nano Lett.* **2014**, *14*, 2105−2110.

(13) Guo, C. F.; Liu, Q.; Wang, G.; Wang, Y.; Shi, Z.; Suo, Z.; Chu, C.-W.; Ren, Z. Fatigue-Free, Superstretchable, Transparent, and Biocompatible Metal Electrodes. *Proc. Natl. Acad. Sci. U. S. A.* **2015**, *112*, 12332−12337.

(14) Gao, T.; Haghanifar, S.; Lindsay, M. G.; Lu, P.; Kayes, M. I.; Pafchek, B. D.; Zhou, Z.; Ohodnicki, P. R.; Leu, P. W. Fundamental Performance Limits and Haze Evaluation of Metal Nanomesh Transparent Conductors. *Adv. Opt. Mater.* **2018**, *6*, 1700829.

(15) Wu, J.; Becerril, H. A.; Bao, Z.; Liu, Z.; Chen, Y.; Peumans, P. Organic Solar Cells with Solution-Processed Graphene Transparent Electrodes. *Appl. Phys. Lett.* **2008**, *92*, 263302.

(16) Wu, J.; Agrawal, M.; Becerril, H. A.; Bao, Z.; Liu, Z.; Chen, Y.; Peumans, P. Organic Light-Emitting Diodes on Solution-Processed Graphene Transparent Electrodes. *ACS Nano* **2010**, *4*, 43−48.

(17) Gustafsson, G.; Cao, Y.; Treacy, G.; Klavetter, F.; Colaneri, N.; Heeger, A. Flexible Light-Emitting Diodes Made from Soluble Conducting Polymers. *Nature* **1992**, *357*, 477.

(18) Wang, Y.; Zhu, C.; Pfattner, R.; Yan, H.; Jin, L.; Chen, S.; Molina-Lopez, F.; Lissel, F.; Liu, J.; Rabiah, N. I.; et al. A Highly Stretchable, Transparent, and Conductive Polymer. *Science advances* **2017**, *3*, No. e1602076.

(19) Wu, H.; Kong, D.; Ruan, Z.; Hsu, P.-C.; Wang, S.; Yu, Z.; Carney, T. J.; Hu, L.; Fan, S.; Cui, Y. A Transparent Electrode Based on a Metal Nanotrough Network. *Nat. Nanotechnol.* **2013**, *8*, 421−425.

(20) Kang, H.; Jung, S.; Jeong, S.; Kim, G.; Lee, K. Polymer-Metal Hybrid Transparent Electrodes for Flexible Electronics. *Nat. Commun.* **2015**, *6*, 6503.

(21) Gao, T.; Huang, P.-S.; Lee, J.-K.; Leu, P. W. Hierarchical Metal Nanomesh/Microgrid Structures for Ordered and Uniform Transparent Electrodes. *RSC Adv.* **2015**, *5*, 70713−70717.

(22) Jang, H. Y.; Lee, S.-K.; Cho, S. H.; Ahn, J.-H.; Park, S. Fabrication of metallic nanomesh: Pt nano-mesh as a proof of concept for stretchable and transparent electrodes. *Chem. Mater.* **2013**, *25*, 3535−3538.

(23) Gui, C.; Ding, X.; Zhou, S.; Gao, Y.; Liu, X.; Liu, S. Nanoscale Ni/Au wire grids as transparent conductive electrodes in ultraviolet light-emitting diodes by laser direct writing. *Opt. Laser Technol.* **2018**, *104*, 112−117.

(24) Van Osch, T. H.; Perelaer, J.; de Laat, A. W.; Schubert, U. S. Inkjet Printing of Narrow Conductive Tracks on Untreated Polymeric Substrates. *Adv. Mater.* **2008**, *20*, 343−345.

(25) Scheideler, W. J.; Smith, J.; Deckman, I.; Chung, S.; Arias, A. C.; Subramanian, V. A robust, gravure-printed, silver nanowire/metal oxide hybrid electrode for high-throughput patterned transparent conductors. *J. Mater. Chem. C* **2016**, *4*, 3248−3255.

(26) Schneider, J.; Rohner, P.; Thureja, D.; Schmid, M.; Galliker, P.; Poulikakos, D. Electrohydrodynamic Nanodrip Printing of High Aspect Ratio Metal Grid Transparent Electrodes. *Adv. Funct. Mater.* **2016**, *26*, 833−840.

(27) Zhou, L.; Xiang, H.-Y.; Shen, S.; Li, Y.-Q.; Chen, J.-D.; Xie, H.-J.; Goldthorpe, I. A.; Chen, L.-S.; Lee, S.-T.; Tang, J.-X. High-performance Flexible Organic Light-Emitting Diodes Using Embedded Silver Network Transparent Electrodes. *ACS Nano* **2014**, *8*, 12796−12805.

(28) Chen, X.; Guo, W.; Xie, L.; Wei, C.; Zhuang, J.; Su, W.; Cui, Z. Embedded Ag/ni Metal-Mesh with Low Surface Roughness as Transparent Conductive Electrode for Optoelectronic Applications. *ACS Appl. Mater. Interfaces* **2017**, *9*, 37048−37054.

(29) Rosker, E. S.; Barako, M. T.; Nguyen, E.; DiMarzio, D.; Kisslinger, K.; Duan, D.-W.; Sandhu, R.; Goorsky, M. S.; Tice, J. Approaching the Practical Conductivity Limits of Aerosol Jet Printed Silver. *ACS Appl. Mater. Interfaces* **2020**, *12*, 29684−29691.

(30) Chen, K.; Delicado, P.; Müller, H.-G. Modelling Function-Valued Stochastic Processes, with Applications to Fertility Dynamics. *Journal of the Royal Statistical Society Series B* **2017**, *79*, 177−196.

(31) Sekine, T.; Fukuda, K.; Kumaki, D.; Tokito, S. Enhanced adhesion mechanisms between printed nano-silver electrodes and underlying polymer layers. *Nanotechnology* **2015**, *26*, 321001.

(32) Walker, S. B.; Lewis, J. A. Reactive Silver Inks for Patterning High-Conductivity Features at Mild Temperatures. *J. Am. Chem. Soc.* **2012**, *134*, 1419−1421.

(33) Horváth, B.; Křivová, B.; Schift, H. Nanoimprint meets microfluidics: development of metal wires from nanoparticle ink filled capillaries. *Micro and Nano Engineering* **2019**, *3*, 22−30.

(34) Khan, A.; Lee, S.; Jang, T.; Xiong, Z.; Zhang, C.; Tang, J.; Guo, L. J.; Li, W.-D. High-Performance Flexible Transparent Electrode with an Embedded Metal Mesh Fabricated by Cost-Effective Solution Process. *Small* **2016**, *12*, 3021−3030.

(35) Li, Y.; Meng, L.; Yang, Y. M.; Xu, G.; Hong, Z.; Chen, Q.; You, J.; Li, G.; Yang, Y.; Li, Y. High-Efficiency Robust Perovskite Solar Cells on Ultrathin Flexible Substrates. *Nat. Commun.* **2016**, *7*, 10214.

(36) Hsu, P.-C.; Wang, S.; Wu, H.; Narasimhan, V. K.; Kong, D.; Ryoung Lee, H.; Cui, Y. Performance Enhancement of Metal Nanowire Transparent Conducting Electrodes by Mesoscale Metal Wires. *Nat. Commun.* **2013**, *4*, 2522.

(37) Bae, S.; Kim, H.; Lee, Y.; Xu, X.; Park, J.-S.; Zheng, Y.; Balakrishnan, J.; Lei, T.; Ri Kim, H.; Song, Y. I.; Kim, Y.-J.; Kim, K. S.; Özyilmaz, B.; Ahn, J.-H.; Hong, B. H.; Iijima, S. Roll-to-roll production of 30-in. graphene films for transparent electrodes. *Nat. Nanotechnol.* **2010**, *5*, 574.

(38) Li, L.; Zhang, B.; Zou, B.; Xie, R.; Zhang, T.; Li, S.; Zheng, B.; Wu, J.; Weng, J.; Zhang, W.; Huang, W.; Huo, F. Fabrication of Flexible Transparent Electrode with Enhanced Conductivity from Hierarchical Metal Grids. *ACS Appl. Mater. Interfaces* **2017**, *9*, 39110−39115.

(39) De, S.; Coleman, J. N. Are There Fundamental Limitations on the Sheet Resistance and Transmittance of Thin Graphene Films? *ACS Nano* **2010**, *4*, 2713−2720.

(40) *Standard test method for haze and luminous transmittance of transparent plastics*; ASTM D1003-13; ASTM International: West Conshohocken, PA, 2013.

(41) Kim, K.-B.; Tak, Y.-H.; Han, Y.-S.; Baik, K.-H.; Yoon, M.-H.; Lee, M.-H. Relationship between surface roughness of indium tin oxide and leakage current of organic light-emitting diode. *Jpn. J. Appl. Phys.* **2003**, *42*, L438.

(42) Leterrier, Y.; Médico, L.; Demarco, F.; Månson, J.-A.; Betz, U.; Escolà, M.; Kharrazi Olsson, M. K.; Atamny, F. Mechanical Integrity of Transparent Conductive Oxide Films for Flexible Polymer-Based Displays. *Thin Solid Films* **2004**, *460*, 156−166.

(43) Dong, Q.; Hara, Y.; Vrouwenvelder, K. T.; Shin, K. T.; Compiano, J. A.; Saif, M.; Lopez, R. Superflexibility of Ito Electrodes via Submicron Patterning. *ACS Appl. Mater. Interfaces* **2018**, *10*, 10339−10346.

(44) Beams, J.; Breazeale, J.; Bart, W. Mechanical Strength of Thin Films of Metals. *Phys. Rev.* **1955**, *100*, 1657.

(45) Dai, Z.; Yadavalli, S. K.; Hu, M.; Chen, M.; Zhou, Y.; Padture, N. P. Effect of Grain Size on the Fracture Behavior of Organic-Inorganic Halide Perovskite Thin Films for Solar Cells. *Scr. Mater.* **2020**, *185*, 47−50.

(46) Haghanifar, S.; Galante, A. J.; Leu, P. W. Challenges and Prospects of Bio-Inspired and Multifunctional Transparent Substrates and Barrier Layers for Optoelectronics. *ACS Nano* **2020**, *14*, 16241−16265.